Z. Kristallogr. **221** (2006) 319–333 / **DOI** 10.1524/zkri.2006.221.5–7.319

Preparation, phase stability and structure of the C36 Laves phase $Nb_{1-x}Co_{2+x}$

Daniel Grüner[I], Frank Stein[II], Martin Palm[II], Joachim Konrad[II], Alim Ormeci[I], Walter Schnelle[I], Yuri Grin[I] and Guido Kreiner*, [I]

[I] Max-Planck-Institut für Chemische Physik fester Stoffe, Nöthnitzer Str. 40, 01187 Dresden, Germany
[II] Max-Planck-Institut für Eisenforschung GmbH, Max-Planck-Str. 1, 40237 Düsseldorf, Germany

In commemoration of the 100th anniversary of Fritz Laves' birthday

Received September 16, 2005; accepted December 15, 2005

Laves phases / Niobium / Cobalt / Phase diagram / Single crystal structure analysis / X-ray diffraction

Abstract. The C36 Laves phase $Nb_{1-x}Co_{2+x}$ has been re-investigated in order to study phase stability and structure. Constitutional data have been obtained by investigating homogenized single- and two-phase samples and from diffusion couples. The C36 phase $Nb_{1-x}Co_{2+x}$ crystallizes with hexagonal $MgNi_2$ structure type ($Z = 8$, space group $P6_3/mmc$, $a = 4.7414(4)$ Å and $c = 15.458(1)$ Å at $x = 0.265(4)$). The homogeneity range extends from 24.6(2) to 25.3(5) at% Nb. The temperature range of the phase field is limited by a eutectoid (C36 $Nb_{1-x}Co_{2+x} = Nb_2Co_7$ + C15 $NbCo_2$) and a peritectic (L + C15 $NbCo_2$ = C36 $Nb_{1-x}Co_{2+x}$) reaction at ≈1050 °C and 1264 °C, respectively. In addition, the title phase is involved in the peritectoid reaction Co(Nb) + C36 $Nb_{1-x}Co_{2+x} = Nb_2Co_7$ at 1086 °C and in the eutectic reaction L = Co(Nb) + C36 $Nb_{1-x}Co_{2+x}$ at 1239 °C. The C36 and C15 Laves phases of the Nb–Co system are separated by an extremely small two-phase field (<0.5 at%). The crystal structure exhibits pronounced deviations from ideal parameters obtained from a hard sphere model. The Co network displays a type of distortion known from many hexagonal Laves phases. Kagomé layers display an elongation of the Co–Co edges of the basal triangles of Co_5 trigonal bipyramids and a contraction of Co–Co edges of the uncapped triangles. The Nb atoms are also displaced from their idealized sites. In the crystal structure of C36 $Nb_{1-x}Co_{2+x}$ excess Co atoms randomly substitute Nb atoms – $(Nb_{1-x}Co_x)Co_2$. The excess Co atoms occupy preferentially the Nb2 site approximately twice as much as Nb1. These positions differ mainly in the conformation of the corresponding Nb_6Nb_2 fragments (Nb1–Nb1 eclipsed and Nb2–Nb2 staggered). In addition, Co atoms are displaced from the original Nb positions. The distortion of the Co and the Nb network is a consequence of the bonding situation of the defect-free crystal structure. The preferential site occupation of excess Co atoms is triggered by interactions with atoms beyond the first coordination shell. The C36 phase $Nb_{1-x}Co_{2+x}$ exhibits Pauli-paramagnetic behavior ($\chi_P = +1.31 \cdot 10^{-3}$ emu mol^{-1}). The temperature dependent part of the electrical resistivity $\varrho(300\ K) - \varrho_0$ is only 17 μΩ cm whereas the residual resistivity is very large with $\varrho_0 = 140$ μΩ cm indicating strong structural disorder.

Introduction

Laves phases have the ideal composition AB_2 and form one of the largest groups of intermetallic compounds with more than 1400 known examples. The assignment of an intermetallic compound to the class of Laves phases is based only on geometrical principles of the corresponding crystal structure. Laves phases crystallize in three structure types: cubic $MgCu_2$ (C15), hexagonal $MgZn_2$ (C14) and hexagonal $MgNi_2$ (C36). In the first half of the last century it was shown in the pioneering works of J.B. Friauf [1, 2], F. Laves [3, 4], G. E. R. Schulze [5], F. C. Frank and J. S. Kasper [6, 7], that the Laves phases can be regarded as tetrahedrally close packed (t.c.p) structures of components A and B with tetrahedral interstices only. The ideal ratio of the radii based on a hard-sphere model is $r_A/r_B = \sqrt{(3/2)}$ with two kinds of coordination type polyhedra. The Frank-Kasper polyhedron Z16 surrounding the A atoms has 4 six-fold A vertices and 12 five-fold B vertices, whereas the icosahedron surrounding the B atoms has 6 five-fold A and B vertices. The structure types C15, C14 and C36 can be regarded as polytypes with c_3, h_2, and $(ch)_2$ stacking sequences in Jagodzinski-Wyckoff notation [8] of one common slab composed of tetrahedra and truncated tetrahedra [9]. The Laves phases as a subset of the Frank-Kasper phases can also be described by a stacking of hexagon-triangle layers and triangular layers parallel (001) planes or by a stacking of pentagon-triangle and triangular layers parallel (110) planes of the hexagonal unit cell [6, 7]. Alternatively, a description based on three-dimensional networks is frequently used. The A network

* Correspondence author (e-mail: kreiner@cpfs.mpg.de)

forms a four-connected network interpenetrated by a six-connected network of the *B* atoms. Approximately 25% of the binary Laves phases exhibit considerable homogeneity ranges [10] giving rise to structural defects.

Laves phases have been studied intensely to understand the fundamental aspects of phase stability. However, simple factors governing the crystal structure type of geometric (r_A/r_B) and electronic (valence electron concentration *vec* and electronegativity difference $\chi_A - \chi_B$) nature have proven to be helpful in predicting the occurrence and stability of the Laves phases only in strictly limited cases [11, 12]. The origin of the homogeneity ranges and the corresponding structural defects are in most cases still puzzling and reflect fundamental problems in the chemistry of intermetallic compounds: The incomplete understanding of the complex chemical bonding situation for intermetallic phases, the tendency to form considerable homogeneity ranges and the influence of small amounts of impurities on stability and properties. To address these problems studies on a number of alloy systems with $A = \text{Nb}$ and $B = \text{Cr, Mn, Fe, Co}$ are in progress with experimental and theoretical methods. The goal of the study is to achieve an understanding of the interplay between chemical bonding and phase stability for the Laves phases based on accurate experimental data.

The binary system Nb−Co is particularly suitable to throw light on the stability of the polytypes due to the coexistence of the C15, C14 and C36 Laves phases. The Nb−Co phase diagram has been studied in a number of investigations [13−21]. According to the latest assessment [21], the homogeneity range of the C15 Laves phase extends from 27.1 to 33.4 at% Nb, asymmetrically enclosing the composition $NbCo_2$. The phase is stable up to 1475 °C where it melts congruently. The C14 Laves phase forms off-stoichiometrically on the Nb-rich side and has a narrow homogeneity range, the shape of which is virtually unknown. It is a high-temperature phase which is reported to be stable between 1212 °C and 1428 °C. Finally, a phase with C36 structure type is reported to be another high-temperature phase stable from 1005 °C to 1249 °C close to the composition $NbCo_3$, *i.e.*, strongly off-stoichiometric [14, 15]. For both the C14 and the C36 Laves phases no exact information on the homogeneity range is available. In addition to the Laves phases and the two terminal solid solutions Co(Nb) and Nb(Co), a μ-phase Nb_6Co_7 and a phase close to the composition Nb_2Co_7 with hitherto unknown crystal structure have been reported. The homogeneity range of the congruently melting phase Nb_6Co_7 extends from 50.4 to 53.3 at% Nb. Nb_2Co_7 forms in a peritectoid reaction from Co(Nb) and $NbCo_3$ at 1040 °C [21].

Here, we report results of a detailed investigation on the phase stability, structural defects, and chemical bonding of the C36 Laves phase in the Nb−Co system.

Experimental section

Synthesis and chemical analysis

To check the starting materials for impurities, chemical analysis was performed using the carrier gas hot extraction or the combustion technique for non-metal impurities (H: Leco RH-402; N, O: Leco TC-436 DR; C: Leco C-200 CHLH) and for metal impurities by Inductively Coupled Plasma Mass Spectrometry (ICP-MS, Varian). Si (300 ppm), Fe (33 ppm), and Zn (7 ppm) have been determined as the main impurities in case of the Co-foil and Ta (290 ppm), K (210 ppm), and W (50 ppm) in case of the Nb-granules. The concentration of other metallic elements turned out to be below the respective limit of detection (LOD). The oxygen content of the starting materials was below the respective LOD for Co (0.05 wt%) and Nb (0.025 wt%).

Samples of Nb and Co with nominal composition of 23.0, 24.0, 25.0, 25.2, 25.5, 26.0, 27.0, and 28.0 at% Nb, each of approx. 2 g mass, were prepared by arc-melting (Centorr Series 5BJ, Centorr Vacuum Industries) from the elements (Nb, H. C. Starck, granules, 99.9%; Co, Chempur, foil, 99.995%) on a water-cooled copper hearth in argon atmosphere.

Prior to the preparation the argon atmosphere inside the arc-melter has been purified by melting an ingot of titanium several times in an adjacent recess of the copper hearth. To assure homogeneity all samples have been turned over and remelted several times. The weight loss after arc-melting was smaller than 0.1 wt%. Finally, the reguli were enclosed in weld-sealed niobium ampoules (Plansee AG, $\varnothing = 10$ mm) which were encapsulated in fused silica tubes filled with argon (≈250 mbar). After annealing at 1100 °C for one month, the samples were quenched in cold water.

For the investigation of the sample composition, atomic emission spectrometry with plasma excitation (ICP-OES, Varian, Vista RL) was used. For each analysis ≈20 mg of the material were dissolved in a mixture of hydrofluoric and nitric acid. Furthermore, to exclude any possibility of contamination during the preparation each specimen was analyzed for H, N, O, and C impurities as explained above. All non-metallic impurities after preparation were below their respective LOD.

Phase analysis

For metallographic examination, pieces of about 5 mm diameter were embedded in epoxy resin. Grinding was performed using fixed abrasive papers (500 and 1000-grit silicon carbide) and water as lubricant. Polishing was done using a slurry of 9 and 3 μm diamond powders in water and a mixture of 80% ethyl alcohol, 10% propyl alcohol and 10% ethylene glycol as lubricant. For the final polishing step, colloidal silica (≈0.05 μm) in water has been used. After each step the specimens were cleaned with water. The microstructures were examined optically and with a scanning electron microscope (Zeiss Axioplan 2 and Philips SL30, respectively). The compositions of the observed phases were analyzed by EDXS (Philips XL30) and WDXS (Cameca SX 100) using elemental Nb and Co as standards.

The unit cell parameters at room temperature were determined from X-ray powder diffraction data employing a Huber G670 Guinier-camera equipped with a Ge monochromator and CoK_{α_1} radiation ($\lambda = 1.78897$ Å). Silicon (National Institute of Standards & Technology (NIST)

SRM 640c, $a = 5.43119(1)$ Å) or LaB_6 (NIST SRM 660a, $a = 4.15692(1)$ Å) were used as internal standards. The unit cell parameters were refined by least-squares fits of the diffraction angles in the range $20° \leq 2\theta \leq 100°$ where 2θ is the diffraction angle using the program PPLP of the NRCVAX suite [22]. Powder diffraction intensities were calculated using the program WINXPOW [23].

DTA/DSC measurements (STA 449 C, thermocouple type S; HT-DSC 404 C, Netzsch and SETSYS16/18, Setaram) were carried out on powdered samples with nominal compositions $Nb_{15}Co_{85}$, $Nb_{22.2}Co_{77.8}$, and $Nb_{24}Co_{76}$ in alumina crucibles in the temperature range from 250 °C to 1500 °C to obtain the temperatures of the invariant reactions. A heating/cooling rate of 10 K/min has been applied. For temperature calibration the melting points of five pure metals have been used.

Diffusion couples were prepared from slices of pure Co and pure Nb or of pure Co and the C15 $NbCo_2$ Laves phase. The contact faces were ground and polished down to 1 μm. The contacted pieces were put into a small closed alumina crucible which was wrapped with Nb foil. The crucible was inserted upside down into a larger alumina crucible and the space between the two crucibles was filled with fine pieces of titanium as getter material. Heat treatments were performed at temperatures between 1020 °C and 1230 °C for 72 to 40 h in an argon atmosphere.

The resulting concentration profiles were analyzed by electron-probe microanalysis. Phase analysis was performed in a high-resolution field emission scanning electron microscope (JEOL JSM 6500 F) equipped with a high-speed electron back-scatter diffraction (EBSD) system by TSL.

Magnetism and electrical resistivity

The magnetization was measured in external magnetic fields of 3.5 and 7 T in a SQUID magnetometer (MPMS XL-7, Quantum Design) in the temperature range 1.8–400 K for single-phase samples of nominal composition $Nb_{25.0}Co_{75.0}$ and $Nb_{25.2}Co_{74.8}$ (no. 3 and no. 4, respectively, in Table 1). The electrical resistivity of single-phase $Nb_{25.0}Co_{75.0}$ (no. 3 in Table 1, prismatic shape, 0.39 mm 0.37 mm × 2.2 mm) was measured by a standard dc four point method in the temperature range 4–320 K.

X-ray structure analysis

A single crystal of irregular shape and metallic luster was selected from a crushed specimen of the nominal composition $Nb_{24}Co_{76}$ (no. 2 in Table 1), mounted onto a Lindemann glass fibre, and checked with Laue photographs. The single crystal data collection was carried out with a Rigaku AFC7 diffractometer equipped with a Mercury CCD detector with MoK_α radiation ($\lambda = 0.71073$ Å). Laue symmetry (6/*mmm*) and extinction class (*P*–*c*) reveal the possible space groups $P6_3/mmc$ (no. 194), $P\overline{6}2c$ (no. 190) and $P6_3mc$ (no. 186). Lorentz-polarization and numerical absorption correction were done using the program CrystalClear [24]. For averaging of symmetrically equivalent reflections and full-matrix-block least-squares refinements on F^2 the program SHELXL97 [25] and for calculations of the Fourier maps the Windows version of the CSD [26] program package and JANA2000 [27] have been applied. The averaging procedure in 6/*mmm* yielded 226 unique reflections with $R_{int} = 0.029$, among them 218 observed with $I > 2\sigma(I)$.

Computational methods

Electronic structure and phase stability of the $Nb_{1-x}Co_{2+x}$ phase with the C36 structure type are studied by the all-electron, full-potential local orbital (FPLO) [28] minimum basis method within the local density approximation [29] to density functional theory [30]. The basis functions in the FPLO method are nonorthogonal and they are obtained numerically by solving a Schrödinger equation which includes a confining potential [31] for states treated as valence. The confining potential compresses the valence functions in order to make them local. In our calculations the basis orbital set for Nb consisted of 4*s*, 4*p*, 5*s*, 5*p*, 4*d*, 4*f* states while for Co the states 3*s*, 3*p*, 4*s*, 4*p*, 3*d* were used. The semicore states 4*s*, 4*p* of Nb and 3*s*, 3*p* of Co together with the polarization state 4*f* of Nb were calculated with fixed compression. For the remaining states the compression parameters were optimized during the self-consistency cycles. The Perdew-Wang [32] parameterization of the exchange-correlation functional was used. The Brillouin zone integrations were carried out by the tetrahedron method.

We also used the Stuttgart tight-binding linear muffin-tin-orbital method in the atomic sphere approximation (TB-LMTO-ASA) [33] in order to study the reasons for the observed distortions and site occupancies. In TB-LMTO-ASA calculations combined-correction terms were included and the sphere radii were determined automatically by the program.

Results and discussion

Phase analysis

Table 1 gives a summary of the results of the phase analysis. A schematic section of the Nb–Co phase diagram based on compositional and thermal data of this study is shown in Fig. 1. The C36 Laves phase $Nb_{1-x}Co_{2+x}$ forms in a narrow homogeneity range close to $x \approx 0.25$ ($NbCo_3$). Alloys with nominal compositions of 24 at% Nb and below annealed at 1100 °C show mixtures of Co(Nb) + C36 Laves phase, alloys with 25.5 and 26 at% Nb are two-phase alloys C36 + C15. At Nb contents above 26 at%, single-phase alloys with C15 structure type were obtained. The lattice parameters *a* and *c* of the hexagonal unit cell are plotted versus the nominal composition in Fig. 2. Due to the extremely narrow homogeneity range of the C36 Laves phase and the small two-phase field C36 + C15, only a small number of data points are available. An extrapolation of the single-phase and two-phase portions of the curves in Fig. 2 to their points of intersection gives the compositions at the C36 phase boundaries as 24.9(5) and

Table 1. Summary of phase analysis for Nb−Co alloys after annealing at 1100 °C and subsequent quenching.

No.	Phases	Nb content (at.%) Nominal	ICP-OES	WDXS	Unit cell parameters *a*, *c* of the C36 phase (Å)
1	Co(Nb) + C36	23.0	–	–	4.7415(8), 15.459(3)
2	Co(Nb) + C36	24.0	24.3(3)	C36: 25.14(5)	4.7414(4), 15.458(1)
3	C36 + traces of Co(Nb)	25.0	25.0(2)	C36: 25.9(1)	4.743(1), 15.462(4)
4	C36	25.2	24.9(4)	–	4.745(1), 15.471(4)
5	C15 + C36	25.5	–	–	
6	C15 + C36	26.0	–	C15: 26.7(1)	4.747(2), 15.484(7)
7	C15 + traces of C36	27.0	–	–	
8	C15	28.0	27.1(2)	C15: 28.3(1)	

25.5(5) at% Nb, which corresponds to a homogeneity range of 0.6 at%.

For a more detailed investigation of the C36 phase field and the C15 + C36 two-phase region, several diffusion couples, composed of the cubic $NbCo_2$ Laves phase of stoichiometric composition together with pure Co or of pure Nb together with pure Co, were annealed at temperatures between 1150 and 1230 °C. A respective concentration profile (Fig. 3) shows the steep concentration step between the Co(Nb) solid solution and the Laves phase with a composition typical for the C36 polytype. Concentrations obtained for this Co-rich boundary of the Laves phase field are 24.6, 24.6, 24.5, and 24.5 at% Nb at 1150, 1205, 1215, and 1230 °C, respectively. However, no concentration step is visible which would indicate the transition from the C36 to the C15 phase. The two-phase field must be too narrow to be detected in the concentration profile, *i.e.*, the step is too small (<0.5 at%) or C36 simply is not present in the diffusion couples. It is well-known that the formation of equilibrium phases may be hindered in diffusion couples due to kinetic reasons [34].

In order to solve this problem, the phases in the C15 $NbCo_2$/Co diffusion couple were analyzed by EBSD. A complete phase mapping across the phase boundaries in a strip 30 μm wide was obtained by measuring with a step width of 300 nm. Figure 4 shows an image quality map reflecting the microstructure and color-coded EBSD mappings of the phases and their crystallographic orientations. Four characteristic Kikuchi patterns measured in the different phase fields are also shown. The diffraction bands were indexed using the Hough transformation method. It can be clearly seen that the hexagonal C36 Laves phase has formed in a zone about 20 μm wide between the C15 Laves phase and the *fcc* Co(Nb) solid solution. On the Co-rich side, both the *fcc* and the *hcp* Co(Nb) solid solution are observed. At 1150 °C, the complete region of the Co(Nb) solid solution consists of the *fcc* polymorph. However, during cooling to room temperature the transformation to the *hcp* Co polymorph, which is the stable variant at room temperature, can not be suppressed in the Nb-poor regions, whereas the regions with the higher Nb con-

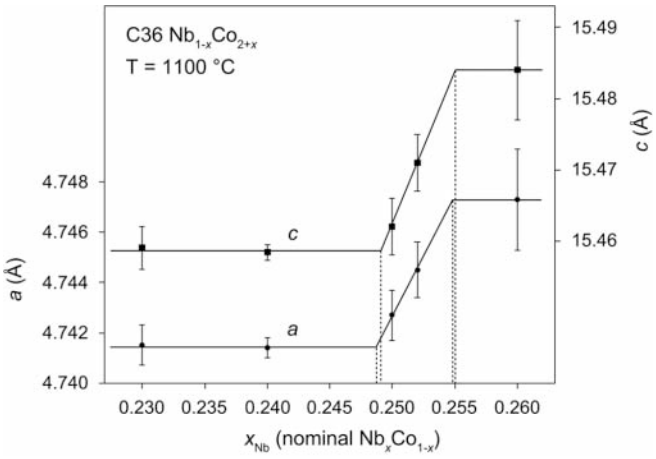

Fig. 2. Unit cell parameters *a* and *c* of the hexagonal C36 $Nb_{1-x}Co_{2+x}$ phase vs. the nominal composition. Phase boundaries at the annealing temperature 1100 °C are given by dashed lines.

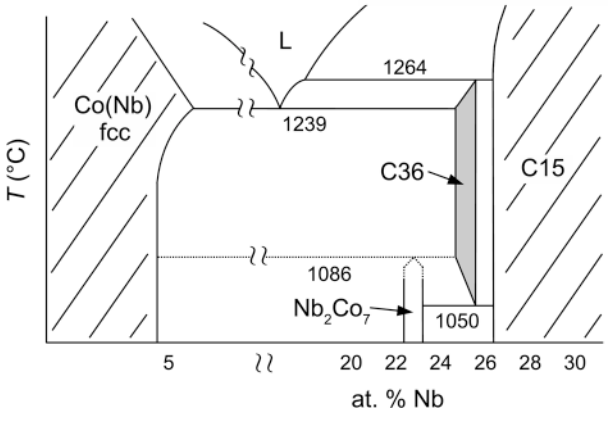

Fig. 1. Schematic drawing of the phase equilibria in the Nb−Co phase diagram (3–30 at% Nb).

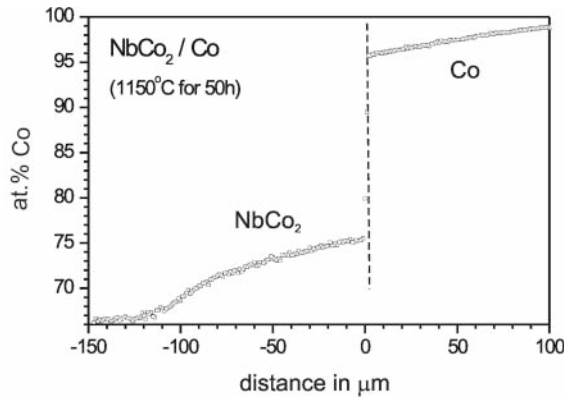

Fig. 3. The concentration profile obtained from a C15 $NbCo_2$/Co diffusion couple (50 h at 1150 °C) by EPMA.

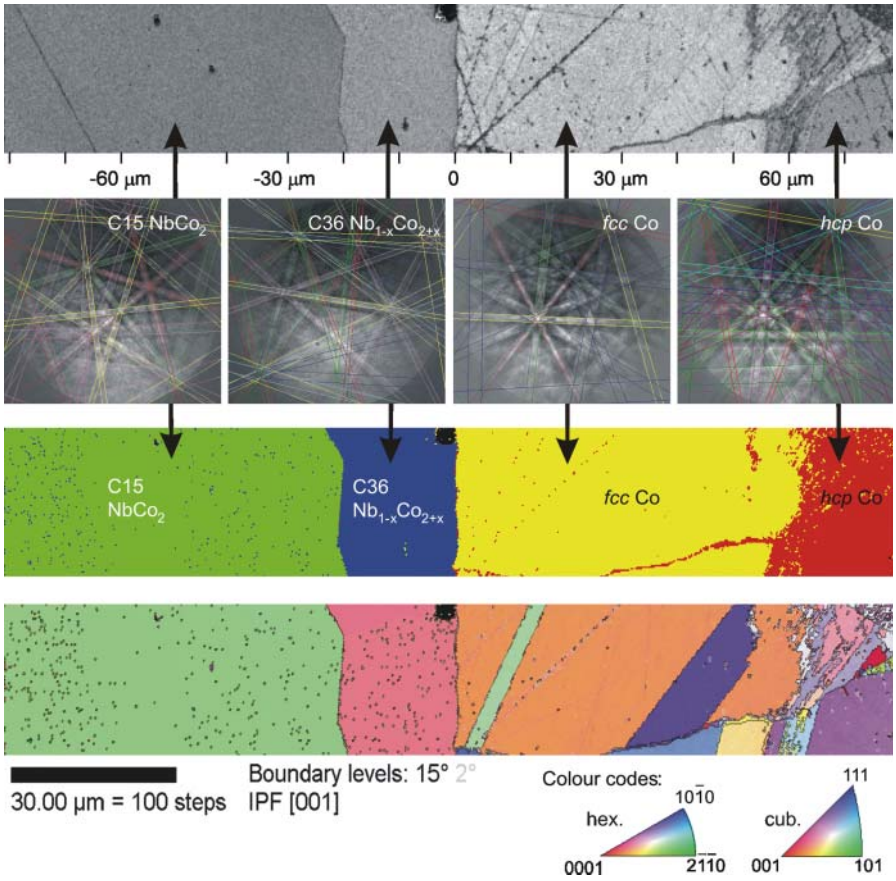

Fig. 4. Results of EBSD investigations of a C15 $NbCo_2$/Co diffusion couple, 50 h at 1150 °C (from top to bottom): image quality map reflecting the microstructure, characteristic Kikuchi patterns of the four phases, color-coded EBSD mappings of the phases and the crystallographic orientations of the grains.

tents metastably remain in the high-temperature *fcc* state. The occurrence of the C36 Laves phase in the diffusion couple confirms that C36 $Nb_{1-x}Co_{2+x}$ is an equilibrium phase of the Nb−Co system as had been found in the investigation of heat-treated alloys of respective compositions, and it can be concluded that the extension of the two-phase field between the C15 and C36 Laves phase polytypes is below 0.5 at%. According to the results obtained from the diffusion couple, the C36 phase field extends from 24.6(2) to 25.3(5) at% at 1150 °C. The width of 0.7(2) at% at 1150 °C excellently fits the value 0.6 at% obtained by extrapolating the unit cell parameters of samples annealed at 1100 °C. The results from the EPMA measurements are more reliable since both values have been obtained from a large number of measurements. In addition, the maximal concentration of Nb for the C36 phase has been determined to be 24.5(4) at% by single crystal structure refinement (see section *structure refinement*). The invariant reactions involving the C36 phase are as follows:

a) L + C15 = C36 peritectic reaction at 1264(2) °C
b) L = Co(Nb) + C36 eutectic reaction at 1239(2) °C
c) Co(Nb) + C36 = Nb_2Co_7 peritectoid reaction at 1086(2) °C
d) C36 = Nb_2Co_7 + C15 eutectoid reaction between 1000 and 1100 °C (≈1050 °C)

The eutectoid decomposition of C36 is too slow to be fixed in the DTA/DSC measurements. However, as an alloy with 24 at% Nb is two-phase (C15 + Nb_2Co_7) after annealing at 1000 °C but consists of C36 + Co(Nb) after annealing at 1100 °C, the eutectoid reaction must occur within this temperature interval.

Structure refinement

As starting parameters the fractional coordinates of the idealized crystal structure of C36 $NbCo_2$ according to the hard sphere model in a standardized description [35] have been used (Table 2).

Least-squares refinement of the positional, occupational, and displacement parameters indicates a partial occupation of the two crystallographically independent Nb1 and Nb2 sites with excess Co atoms. A more detailed analysis of Fourier maps close to the Nb positions reveals a non-spherical electron density distribution which is characteristic for split atom positions (Fig. 5). In case of the Nb1 position (4*f*) the maximum difference density is located on the threefold axis and its occupation corresponds to 0.84 Nb. The additional maxima are displaced from the threefold axis at the Wyckoff position 12*k* and their occupation corresponds to $^{0.16}/_{3}$ Co. Close to the Nb2 position the inspection of the difference electron density also reveals

Table 2. Ideal atomic parameters for a crystal structure of C36 $NbCo_2$ according to the hard sphere model. The ideal *c/a* ratio is $2\sqrt{(^{8}/_{3})} \approx 3.266$. For each crystallographic site layer stacking symbols are given in the last column.

Atom	Site	*x*	*y*	*z*	Symbol[a]
Co1	6*h*	$^{1}/_{6}$	$^{1}/_{3}$	$^{1}/_{4}$	**β**, **γ**
Co2	6*g*	$^{1}/_{2}$	0	0	**α**
Co3	4*f*	$^{1}/_{3}$	$^{2}/_{3}$	$^{1}/_{8}$	**b**, **c**
Nb1	4*f*	$^{1}/_{3}$	$^{2}/_{3}$	$^{21}/_{32}$	**B**, **C**
Nb2	4*e*	0	0	$^{3}/_{32}$	**A**

a: see section *crystal chemistry*

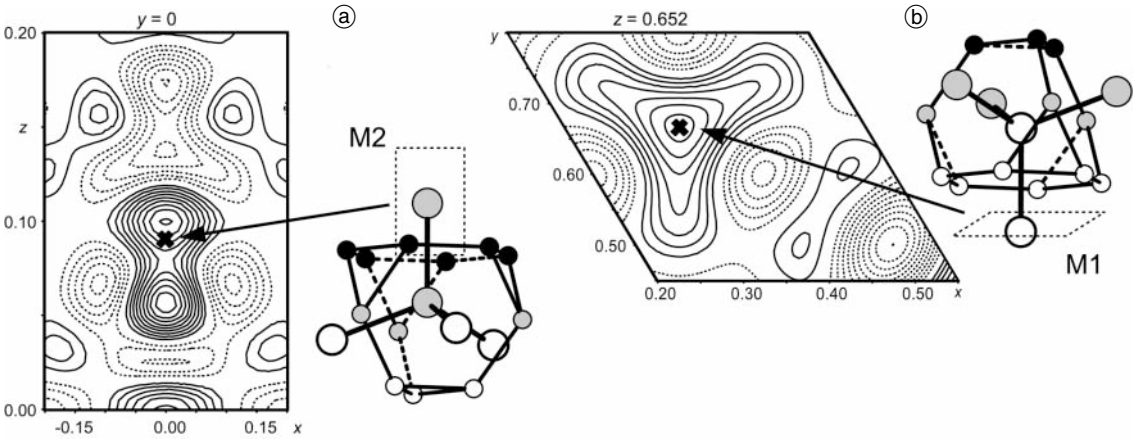

Fig. 5. Difference electron density maps around the M2 (**a**) and M1 (**b**) sites. Position and alignment for both maps are indicated by the rectangle, bordered by a dashed line, in the drawing of the respective coordination polyhedron. A cross marks the idealized position of Nb.

two maxima. The first is assigned to 0.63 Nb and the second to 0.37 Co, 0.116 Å away. In the final cycles of the refinements the split atom positions, hereinafter called M1 = M1a(Nb) + M1b(Co) and M2 = M2a(Nb) + M2b(Co), were constrained to a total of 4 M1 and 4 M2 per unit cell. The thermal parameters of the M1a and M1b positions have been constrained to be equal and the M2 position restricted to isotropic refinement. Reliability factors of the refinement converged to $R_1(F^2) = 0.037$, $wR_2(F^2) = 0.083$ for all reflections. Crystallographic data and details on data collection and structure refinement, atomic coordinates and isotropic and anisotropic displacement parameters are listed in Tables 3, 4 and 5, respectively. Selected interatomic distances are presented in Table 6.

Crystal chemistry

C36 $Nb_{1-x}Co_{2+x}$ crystallizes with hexagonal translational symmetry and 24 atoms per unit cell. The crystal structure reveals two prominent features: distortions of the Nb and the Co network as well as local atomic displacements of the excess Co atoms.

C36 $NbCo_2$ with an idealized crystal structure may be described as a three-dimensional space filling arrangement of empty regular tetrahedra Co_4 and truncated tetrahedra Co_{12} filled with Nb (see Fig. 7). The packing ratio of the two different types of polyhedra is 1:1. The interatomic distance of adjacent atoms occupying nodes of the six-connected Co network is $d(\text{Co–Co}) = 0.5a$. $(Co3)_1(Co2)_3$ tetrahedra are connected to four tetrahedra by corner sharing $(3 \times (Co3)_1(Co2)_3 + 1 \times (Co3)_1(Co1)_3)$. Two $(Co3)_1(Co1)_3$ tetrahedra form trigonal bipyramids (tbps). The axial Co3 atoms of the tbps share corners with $(Co3)_1(Co2)_3$ tetrahedra whereas the equatorial Co atoms are linked with neighboring tbps. The larger Nb atoms occupy the centers of the truncated Co_{12} tetrahedra and form a four-connected Nb network with $d(\text{Nb–Nb}) \approx 0.6124a$. The distance center-to-vertex of the truncated tetrahedron is $d(\text{Nb–Co}) \approx 0.5863a$.

The coordination type polyhedra of Nb and Co are shown in Fig. 6 for C36 $NbCo_2$ with idealized parameters taken from Table 2. The Co atoms are icosahedrally coordinated by 6 Co and 6 Nb atoms as nearest neighbors. Co1 has a boat-like, Co2 a chair-like and Co3 an octahedron-like arrangement of the six Nb neighbors. The coordination type polyhedra of Nb1 and Nb2 are Frank-Kasper polyhedra of coordination number 16 (Z16). They are derived from the Co_{12} truncated tetrahedron by capping each hexagon with Nb.

Another convenient way to describe the C36 structure type is to use a layer description, *i.e.*, by stacking Kagomé and triangular layers along [001]. A Kagomé layer is a hexagon-triangle layer where two triangles and two hexagons meet at each vertex with vertex configuration (3.6.3.6) whereas the triangular layer consists of six triangles meeting at each vertex (3^6). The position of the atoms of the layers relative to the origin of the hexagonal unit cell can be described by the following notation: **A**, $\mathbf{a} = (0, 0, z)$; **B**, $\mathbf{b} = (^2/_3, ^1/_3, z)$; **C**, $\mathbf{c} = (^1/_3, ^2/_3, z)$ for the triangular layers and $\boldsymbol{\alpha} = (^1/_2, 0, z)$; $\boldsymbol{\beta} = (^1/_6, ^1/_3, z)$; $\boldsymbol{\gamma} = (^5/_6, ^2/_3, z)$ for the Kagomé layers. The capital letters **A**, **B**, **C** denote large Nb atoms and small letters **a**, **b**, **c**, **α**, **β**, **γ** small Co atoms. Each greek and latin letter in a sequence denotes 3 and 1 atoms per unit cell, respectively. A similar notation was first introduced by Allen [36]. The layer stacking symbols for the crystallographically different atoms are given in the last column of Table 1. The sequence of layers in a unit cell of the hexagonal C36 structure along [001] is then as follows, with | as symbol denoting the unit cell boundary.

|α A c B β B c A α A b C γ C b A| (see also Fig. 7)

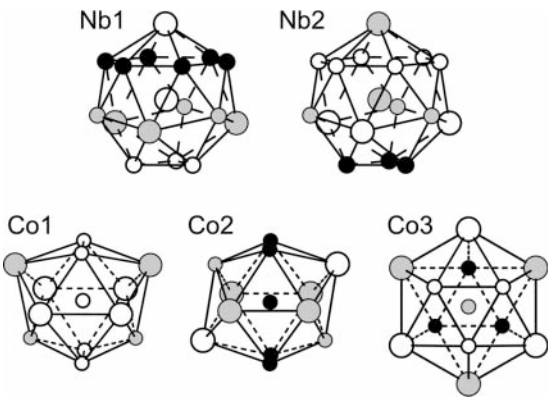

Fig. 6. The coordination type polyhedra of the crystal structure of C36 $NbCo_2$ with idealized parameters as listed in Table 1. Each label denotes the atom type at the center of the respective polyhedron. Large and small spheres represent Nb and Co atoms, respectively.

Table 3. Crystallographic data and details on data collection and structure refinement for $Nb_{1-x}Co_{2+x}$ at $x = 0.265(4)$[a].

Crystal data	
Refined composition	$Nb_{0.735}Co_{2.265(4)}$, 24.5(4) at% Nb
Z	8
Formula mass ($g \cdot mol^{-1}$)	201.77
$F(000)$	730.5
Crystal system	hexagonal
Space group	$P6_3/mmc$ (no. 194)
a (Å)[b]	4.7414(4)
c (Å)[b]	15.458(1)
Volume (Å^3)	300.96(4)
ϱ_{calc} ($g \cdot cm^{-3}$)	8.900
Crystal color	metallic luster
Crystal size (mm^3)	$0.041 \times 0.057 \times 0.064$
Data collection	
Diffractometer system	Rigaku AFC7 Mercury CCD
Radiation type, wave length (Å)	MoK_α, $\lambda = 0.71073$
Monochromator	graphite
Temperature (K)	293(2)
Scan type	φ, ω
Number of images	400, 100
2θ-range	$5.28 \leq 65.54°$
h, k, l range	$-6 \leq h \leq 6$ $-6 \leq k \leq 6$, $-11 \leq l \leq 21$
Absorption correction	numerical
Absrption coefficient, μ (mm^{-1})	29.490
T_{max}, T_{max}	0.561, 0.473
Measured reflections	2361
Unique reflections	226
Observed reflections ($I > 2\sigma(I)$)	218
R_{int}	0.029
Refinement	
Refinement on	F^2
Number of parameters	24
R_1/wR_2 ($I > 2\sigma(I)$)[c]	0.036/0.082
R_1/wR_2 (all data)[c]	0.037/0.083
Goodness-of-fit on F^2	1.257
Extinction coefficient k[d]	0.0058(9)
Min., max. residual peaks ($e \cdot A^{-3}$)	$-1.871, 1.467$

a: Further details of the crystal structure investigation are available from the Fachinformationszentrum Karlsruhe, D-76344 Eggenstein-Leopoldshafen, Germany (fax: +49-7247-808-666; e-mail: crysdata@fiz-karlsruhe.de) on quoting the depository number CSD-415720, the name of the author, and the citation of the paper.
b: From calibrated powder diffraction data.
c: $R_1 = \sum ||F_o| - |F_c|| / \sum |F_o|$; $wR_2 = \sum (w(F_o^2 - F_c^2)^2 / (\sum (F_o^2)^2)^{1/2}$, $w = 1/[\sigma^2(F_o^2) + (0.0347 \cdot P)^2 + 2.6669 \cdot P]$, $P = (\max(F_o^2, 0) + 2F_c^2)/3$.
d: F_c is multiplied by $k[1 + 0.001 \cdot F_c^2 \cdot \lambda^3 / \sin(2\theta)]^{-1/4}$

The sequence **|α β α γ|** denotes Kagomé Co layers at $z = 0$, $^1/_4$, $^1/_2$, $^3/_4$, **|c c b b|** triangular Co layers at $z = ^1/_8$, $^3/_8$, $^5/_8$, $^7/_8$ and **|A B B A A C C A|** triangular Nb layers at $z = ^3/_{32}$, $^5/_{32}$, $^{11}/_{32}$, $^{13}/_{32}$, $^{19}/_{32}$, $^{21}/_{32}$, $^{27}/_{32}$, and $^{29}/_{32}$.

Table 4. Atomic coordinates and equivalent displacement parameters (in Å^2) for $Nb_{1-x}Co_{2+x}$, $x = 0.265(4)$; U_{eq} is defined as one third of the trace of the orthogonalized U_{ij} tensor; E.s.d.'s are given in parentheses.

Atom	Site	x	y	z	U_{eq}/U_{iso}	Occupancy
Co1	6*h*	0.1634(1)	$2x$	$^1/_4$	0.0080(2)	1
Co2	6*g*	$^1/_2$	0	0	0.0088(2)	1
Co3	4*f*	$^1/_3$	$^2/_3$	0.12576(8)	0.0091(3)	1
M1a	4*f*	$^1/_3$	$^2/_3$	0.6551(2)	0.0112(4)[a]	0.84(1) Nb
M1b	12*k*	0.311(2)	$1 - x$	0.652 (2)	0.0112[a]	0.053(4) Co
M2a	4*e*	0	0	0.0927(2)	0.0130(7)[c]	0.63(1)[b] Nb
M2b	4*e*	0	0	0.0852(4)	0.008(1)[c]	0.37 Co[b]

a: U_{ij}(M1a) = U_{ij}(M1b)
b: s.o.f. (M2a) + s.o.f. (M2b) = 1
c: U_{iso}

It has been shown by Samson [9] that two Kagomé layers as top and bottom layers with three intermediate triangular layers, *e.g.* the sequence {**α A c B β**}, represent a thick slab of fused Co_4 and Co_{12} polyhedra, the latter centered by Nb atoms. The structure of the C36 polytype is then described as an intergrowth of one common slab with *chch* stacking sequence per unit cell (in short *ch*, see Fig. 7) in Jagodzinski-Wyckoff notation. The symbol *h* (*c*) is assigned to each slab where the two neighboring slabs are displaced sidewise in the same (opposite) direction and for the same distance. There are four slabs per unit cell. However, due to the space group symmetry of $P6_3/mmc$ the unit cell contains only one symmetrically independent slab. The crystal structures of cubic C15 and hexagonal C14 have stacking sequences c_3 (in short *c*) and h_2 (in short *h*), respectively.

The crystal structure of the title compound is shown in Fig. 7. Nb1 and Nb2 sites are labeled M1 and M2, respectively, to take into account the randomly mixed occupation of these positions by Nb and Co atoms.

The crystal structure of the title compound reveals a distinct distortion of the Co network as shown in Fig. 8.

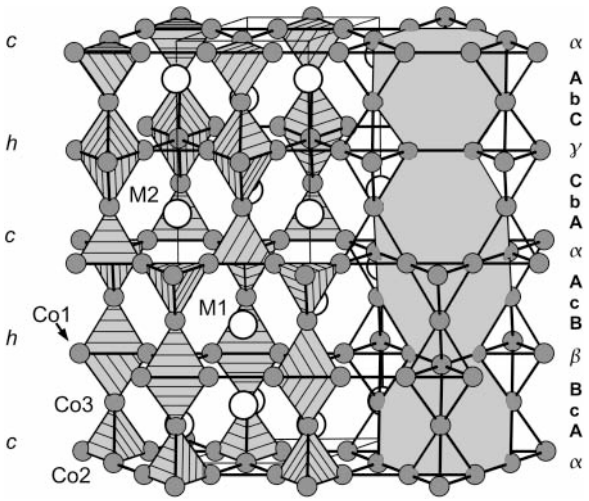

Fig. 7. The crystal structure of C36 $Nb_{1-x}Co_{2+x}$, $x = 0.265$. The stacking sequence of the slabs composed of fused Co_4 and Co_{12} polyhedra and that of the Kagomé and triangular layers is given in Jagodzinski-Wyckoff and "ABC" notation. Local displacements of Nb and Co at M1 or M2 are not displayed.

Table 5. Anisotropic displacement parameters (in Å^2) for $Nb_{1-x}Co_{2+x}$, $x = 0.265(4)$; the general expression of the atomic displacement parameter is exp $[-2\pi^2 \cdot (U_{11} \cdot h^2 \cdot a^{*2} + U_{22} \cdot k^2 \cdot b^{*2} + U_{33} \cdot l^2 \cdot c^{*2} + U_{12} \cdot h \cdot k \cdot a^* \cdot b^* + U_{13} \cdot h \cdot l \cdot a^* \cdot c^* + U_{23} \cdot k \cdot l \cdot b^* \cdot c^*)]$; E.s.d.'s are given in parentheses.

Atom	U_{11}	U_{22}	U_{33}	U_{23}	U_{13}	U_{12}
Co1	0.0090(3)	0.0072(5)	0.0072(4)	0	0	$U_{22}/2$
Co2	0.0100(4)	0.0078(5)	0.0080(4)	0.0006(4)	0.0003(2)	$U_{22}/2$
Co3	0.0105(4)	U_{11}	0.0064(6)	0	0	$U_{22}/2$
M1a, M1b	0.0118(5)	U_{11}	0.0099(5)	0	0	$U_{22}/2$
M2a, M2b[a]	–	–	–	–	–	–

a: isotropic refinement

The $(Co3)_1(Co2)_3$ tetrahedra form a stack of three layers with cubic sequence *c* (Fig. 8a). The corresponding three layer stacks are {**b α c**} or {**c α b**}. The interatomic distances *d*(Co−Co) in the slab are nearly equal, 2.371 Å and 2.378 Å. The $(Co3)_1(Co1)_3$ tetrahedra form a stack of three layers with hexagonal sequence *h*, *i.e.*, {**c β c**} or {**b γ b**} (Fig. 8c).

The interatomic distances *d*(Co−Co) in the cubic slabs are in good agreement with the value of 2.369 Å expected for a crystal structure with ideal structural parameters. This value is obtained from $d(\text{Co–Co}) = \sqrt[3]{V}/(2\sqrt{2})$ where *V* is the unit cell volume of the title compound. The Co−Co distances in the hexagonal slabs are 2.324 Å and 2.417 Å for adjacent atoms of the Kagomé layers and 2.374 Å for adjacent atoms of the Kagomé and neighboring triangular layers. The distortion of the Co network is mainly caused by the distortion of the Kagomé layers (**β** or **γ**) in the hexagonal slabs. The distortion may be described as an elongation of the edges of the basal triangles of the tbps and a contraction of the edges of the uncapped triangles (Fig. 8c).

Table 6. Interatomic distances (in Å) $d < 3.10$ Å for $Nb_{1-x}Co_{2+x}$, $x = 0.265(4)$. E.s.d.'s are given in parentheses. M1a and M2a denote the Nb atoms, while M1b and M2b refer to the excess Co atoms.

Co1–	2	Co1	2.324(2)		
	2	Co1	2.417(2)		
	2	Co3	2.374(1)		
	4	M1a	2.788(1)		
		M1b	2.68(2)/2.82(1)/2.95(2)		
	2	M2a	2.778(2)		
		M2b	2.880(6)		
Co2–	4	Co2	2.3707(2)		
	2	Co3	2.378(1)		
	2	M1a	2.760(2)		
		M1b	2.68(2)/2.82(2)		
	4	M2a	2.770(1)		
		M2b	2.712(3)		
Co3–	3	Co1	2.374(1)		
	3	Co2	2.378(1)		
	3	M1a	2.7747(5)		
		M1b	2.68(1)/2.95(2)		
	3	M2a	2.7848(5)		
		M2b	2.809(1)		
M1a–	3	Co1	2.788(1)		
	6	Co2	2.760(2)		
	3	Co3	2.7747(5)		
	1	M1a	2.935(5)		
		M1b	2.99(2)		
	3	M2a	2.9024(9)		
		M2b	2.943(2)		
M1b–	2	Co1	2.68(2)		
	2	Co1	2.82(1)		
	2	Co1	2.95(2)		
	2	Co2	2.68(2)		
	1	Co2	2.82(2)		
	2	Co3	2.68(1)		
	1	Co3	2.95(2)		
	1	M1a	2.99(2)		
		M1b	3.03(5)/3.04(5)		
	1	M2a	2.71(2)		
		M2b	2.75(2)		
	2	M2a	2.98(1)		
		M2b	3.02(1)		
M2a–	6	Co1	2.778(2)		
	3	Co2	2.770(1)		
	3	Co3	2.7848(5)		
	3	M1a	2.902(1)		
		M1b	2.71(2)/2.98(1)		
	1	M2a	2.865(5)		
		M2b	2.749(4)		
M2b–	3	Co1	2.880(6)		
	6	Co2	2.712(3)		
	3	Co3	2.809(1)		
	3	M1a	2.943(2)		
		M1b	2.75(2)/3.02(1)		
	1	M2a	2.749(4)		
		M2b	2.63(1)		

$d < 2.30$ Å: $d(\text{M1a} - \text{M1b}) = 0.193(1)$ Å, $d(\text{M2a} - \text{M2b}) = 0.116(1)$ Å

In the crystal structure of C36 $NbCo_2$ based on idealized parameters (Table 1) the Nb atoms form a four-connected network with the same topology as found in the crystal structures of 4H−ZnS or carborundum III (SiC) (Fig. 9). The expected distance *d*(Nb−Nb) based on the unit cell volume of the title compound is 2.902 Å. The Nb network may be described as a sequence of double layers {**A A**}−{**B B**}−{**A A**}−{**C C**} in which one Nb atom is vertically above another, *i.e.*, {Nb2 Nb2}−{Nb1 Nb1}−{Nb2 Nb2}−{Nb1 Nb1}. Here, labels Nb1, Nb2 denote the two crystallographically independent Nb sites in the idealized crystal structure. The conformation of ethane-like fragments $Nb_3Nb–NbNb_3$ is either staggered (Nb2−Nb2, Nb2−Nb1) or eclipsed (Nb1−Nb1).

In the crystal structure of the title compound the Nb atoms are displaced from their idealized sites Nb1 and Nb2 to M1a and M2a, respectively. Upon distortion three different interatomic distances $d(\text{M1a–M1a}) = 2.935$ Å, $d(\text{M2a–M2a}) = 2.865$ Å, and $d(\text{M1a–M2a}) = 2.902$ Å are obtained. The distance *d*(M1a−M1a) is longer, *d*(M2a−M2a) shorter and *d*(M1a−M2a) unchanged in comparison to the idealized distance. A snapshot of the distortion of the Nb network is displayed in Fig. 10a.

Excess Co randomly substitutes Nb at both crystallographic sites with a preferred occupation of the Nb2 site (s.o.f.(Co@M2) : s.o.f.(Co@M1) ≈ 2 : 1). No superstructure describing any kind of an ordered arrangement has been observed by X-ray diffraction and there is no evidence of an order-disorder transition to be seen in thermal analysis measurements. Moreover, TEM investigations including HREM, SAED, and CBED techniques on samples of the present study [37] exclude a superstructure. The substitution of the Nb atoms by the smaller Co atoms triggers a local displacement of the excess Co to the M1b and M2b positions (Fig. 10b).

Random substitution, preferred occupation of M2 by Co, and local displacements of Co relative to Nb make the

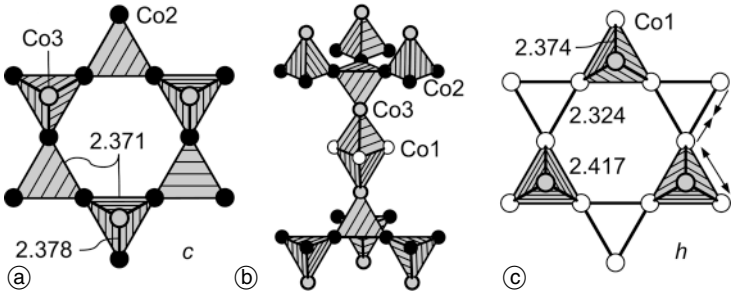

Fig. 8. The Co network of C36 $Nb_{1-x}Co_{2+x}$, $x = 0.265$. (**a**) cubic c arrangement of three sequential layers ({**b α c**} or {**c α b**}). (**b**) part of the Co network including three Kagomé and four triangular layers. (**c**) hexagonal h arrangement of three sequential layers ({**c β c**} or {**b γ b**}). Arrows indicate the distortions relative to ideal atomic positions.

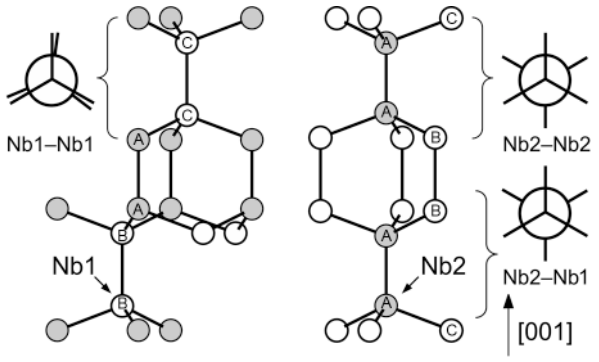

Fig. 9. Part of the Nb network of the crystal structure C36 $NbCo_2$ based on idealized parameters as listed in Table 1. The Nb net may be described as a sequence of double layers {**A A**}–{**B B**}–{**A A**}–{**C C**} with Nb1 at **B**, **C** and Nb2 at **A**. The four-connected net contains ethane-like fragments Nb_3Nb–$NbNb_3$ in either staggered (Nb2–Nb2, Nb2–Nb1) or eclipsed (Nb1–Nb1) conformation.

real structure extremely complicated. The probability distribution for fragments composed of five atoms, M1(M1$M2_3$) and M2(M2$M1_3$), of the A network of C36 $Nb_{1-x}Co_{2+x}$, $x = 0.265$ is shown in Fig. 11. The probability for a specific unit is calculated as the product of the probabilities to find a Co or Nb atom, corresponding to the respective s.o.f., at each of the five sites. *E.g.*, the probability for the top left unit in Fig. 11a is calculated to be s.o.f(M1a)^2 × s.o.f(M2a)^3 = 0.18. Thirty-two different variants of polyhedra for each M1 and M2 are possible ignoring the threefold M1b splitting. In the figure, symmetrically equivalent units are only shown once, but for the calculation of probabilities, all possible units have been considered. The sum of probabilities for each set of units (centered by M1 or M2) is normalized to unity.

Probability distributions p of nearest interatomic distances d(M1–M1), d(M2–M2), d(M1–M2) are listed in Table 7. They are calculated by multiplying the s.o.f. of the respective positions, this time accounting for M1b splitting, and normalizing to the number of M1–M1 (2), M2–M2 (2), M1–M2 (12) contacts per unit cell, respectively. In addition a probability distribution p_{M-M} is given which is nor-

Table 7. Probability distributions for nearest interatomic distances. The probability distributions p give the probabilities for the interatomic distances d with respect to M1–M1, M2–M2, M1–M2, and M–M contacts, respectively.

Type		p_{M1-M1}	p_{M-M}	d (Å)
M1a–M1a	Nb–Nb	0.71	0.08875	2.935
M1a–M1b	Nb–Co	0.27	0.03375	2.99
M1b–M1b	Co–Co	0.007	0.00083	3.03
		0.013	0.00167	3.04
		$\sum = 1$	$\sum = 0.125$	
p_{M2-M2}				
M2a–M2a	Nb–Nb	0.40	0.0500	2.865
M2a–M2b	Nb–Co	0.46	0.0575	2.749
M2b–M2b	Co–Co	0.14	0.0175	2.63
		$\sum = 1$	$\sum = 0.125$	
p_{M1-M2}				
M1a–M2a	Nb–Nb	0.53	0.3975	2.902
M1a–M2b	Nb–Co	0.31	0.2325	2.943
M2a–M1b	Nb–Co	0.03	0.0225	2.71
		0.07	0.0525	2.98
M1b–M2b	Co–Co	0.02	0.0150	2.75
		0.04	0.0300	3.02
		$\sum = 1$	$\sum = 0.75$	

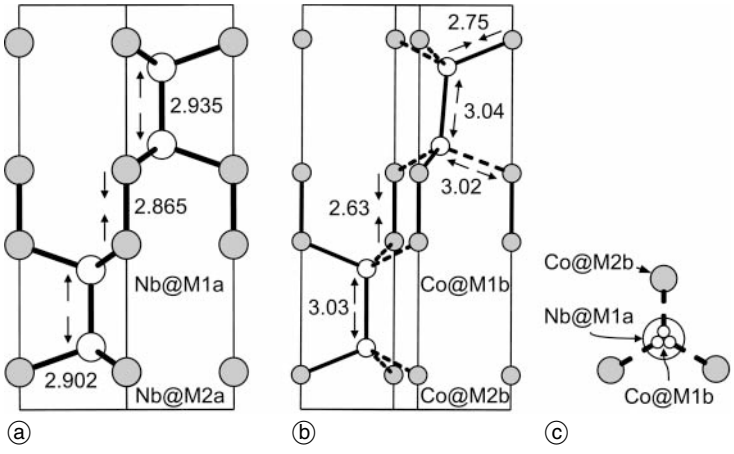

Fig. 10. Distortion of the A network of C36 $Nb_{1-x}Co_{2+x}$, $x = 0.265$. The distortions are indicated by arrows and interatomic distances are given in Å. (**a**): Nb@M1a and Nb@M2a are Nb1 and Nb2 atoms displaced from the idealized crystallographic sites. (**b**) Nb atoms replaced by Co atoms with Co@M1b and Co@M2b displaced from the idealized crystallographic Nb sites. (**c**) Schematic representation of M1$(M2)_3$ fragment with the threefold split position Co@M1b.

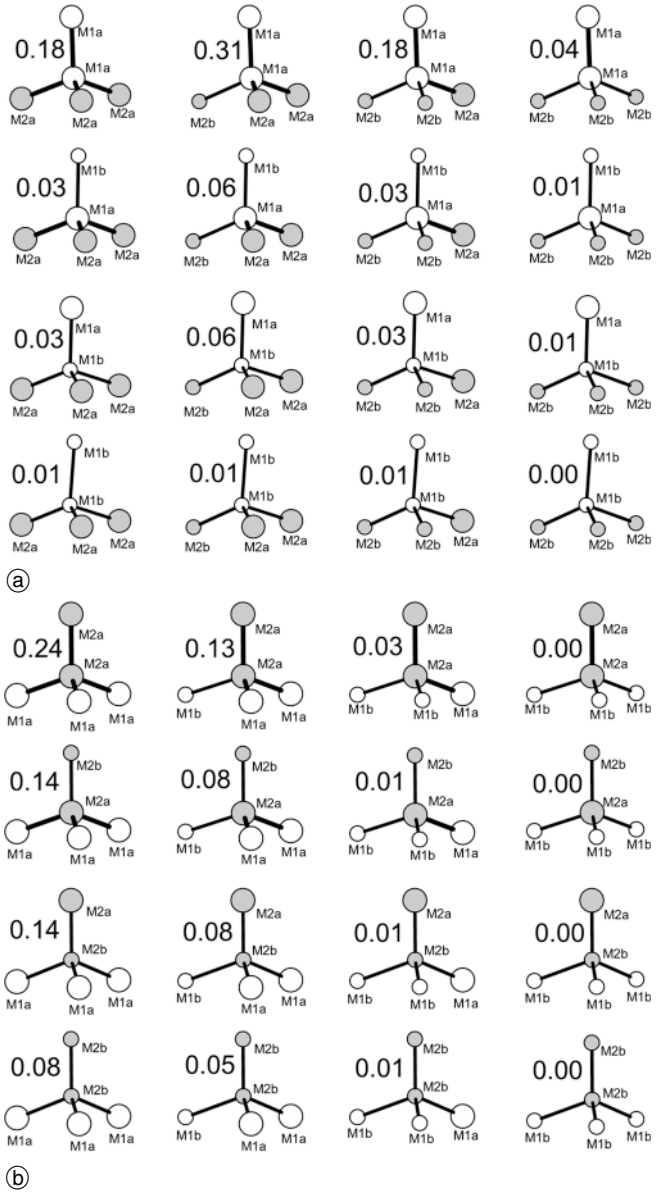

Fig. 11. Probability distributions (**a**) for M1(M1M2$_3$) and (**b**) for M2(M2M1$_3$) fragments of the *A* network of C36 $Nb_{1-x}Co_{2+x}$, $x = 0.265$. For each M1 and M2 sixteen symmetrically distinct polyhedra are possible without accounting for the M1b splitting. The numbers give the probability for each fragment.

malized to the sum (16) of the contacts. The probability to randomize a Co−Co, Nb−Co, and Nb−Nb pair of the *A* network is 0.065, 0.3988 and 0.5362, respectively.

Electronic structure calculations

The experimental data have shown that the C36 polytype of the Nb−Co system is stable at high temperatures in a small homogeneity range close to the composition $NbCo_3$. Structural distortions of *A* and *B* networks and the partial substitution of Nb by Co atoms have turned out to be essential features for the phase stability of C36 $Nb_{1-x}Co_{2+x}$. The experimental findings give rise to fundamental questions concerning the nature of the C36 polytype:

(i) What drives the *A* and *B* network distortion?

(ii) Why is there a non-uniform distribution of the Co atoms among the different crystallographic Nb sites and what determines the observed ratio of $\approx 2:1$.

To gain insight into the origin of the structural distortions and the non-uniform distribution of excess Co atoms on Nb sites quantum mechanical calculations have been performed.

Structural distortions

Structural distortions of the *B* network, i.e., deviations from the ideal structural parameters obtained on the basis of the hard sphere model have been frequently encountered for hexagonal Laves phases, whose atomic positions have been refined [38]. It was shown that the distortion of the *B* network is present even for phases of ideal stoichiometry AB_2, *e.g.*, $MgZn_2$. Since the distortion of the hexagonal slabs in the crystal structure of C36 $Nb_{1-x}Co_{2+x}$ resembles that of many hexagonal Laves phases, one may reason by analogy that this kind of distortion is an inherent structural feature.

According to the present phase diagram, stoichiometric C36 $NbCo_2$ is unstable with respect to C15 $NbCo_2$. However, the stability of C36 $NbCo_2$ with respect to deviations from the idealized crystal structure may be studied by full-potential total-energy calculations. Four atomic coordinates, x(Co1), z(Co3), z(Nb1), z(Nb2), and the unit cell parameters, a and c, are variable. The total energy of C36 $NbCo_2$ has been minimized using the FPLO package [29] by varying the atomic coordinates at the unit cell volume at constant (ideal) value $c/a \approx 3.266$ and composition $NbCo_2$. The starting parameters of the calculation are given in Table 1. The total energy of the best optimized structure is ≈84 J/mol $NbCo_2$ below the energy of the ideal crystal structure. The interatomic distances $d < 3.20$ Å for C36 $NbCo_2$ are listed in Table 8 in comparison with those obtained on the basis of the hard sphere model. The following short notation analogous to that described in [38] has been used. The symbols B_{ij} and A_{ij} denote contacts between neighbors *ij* in the *B* and *A* network, respectively and superscripts u and c distinguish between capped and uncapped triangles of the Kagomé layers. The assignment of the labels B_{ij} and A_{ij} for the respective contacts is illustrated in Fig. 12 for the C36 polytype.

In most cases, the optimization changed the distances towards the experimentally observed values, however, the experimental values were not fully reached. The Kagomé layers of hexagonal slabs display an elongation of the edges ($B_{11}{}^{c}$) of the basal triangles of the tbps and a contraction of the edges of the uncapped triangles ($B_{11}{}^{u}$). In addition, the bond length order $B_{11}{}^{u} < B_{13} < B_{11}{}^{c}$ is in agreement with those reported for the hexagonal Laves phases with refined atomic positions. The optimized value B_{23} is also in good agreement with the observed value. However, B_{13} is calculated to be more or less equal to the ideal value, whereas in the crystal structure it is slightly stretched (0.005 Å). Please note that, the B_{22} value is kept constant due to the applied symmetry restrictions. The interatomic distance A_{22} is noticeably contracted. The behavior of A_{12} is in agreement with the observation, however the change of A_{11} is too small. By introducing the c/a ratio as an additional optimization parameter, one may expect slightly stronger distortions. However, due to the small difference of 0.006 between the ideal and the ob-

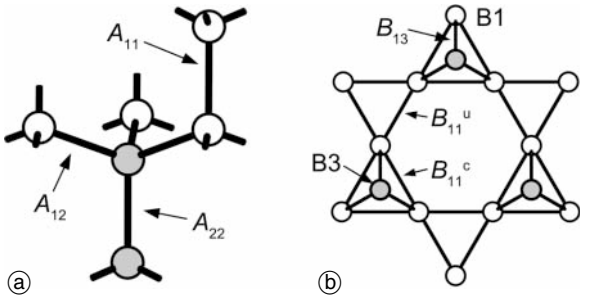

Fig. 12. A short notation for interatomic contacts of the *A* (**a**) and *B* (**b**) network of the C36 Laves phase.

served c/a ratio it is unlikely that full optimization would yield much better values. The large differences between optimized and experimentally observed values show that the substitution may play an important role. Nevertheless, the calculation indicates a tendency of distortion of both the *A* and *B* networks in the crystal structure of hypothetical C36 $NbCo_2$. This conclusion is supported by the observation of a similar distortion in the crystal structure of C36 $NbZn_2$ [39], the latter crystallizing with stoichiometric composition.

In order to study the distortion of the A and the B network in terms of a local bonding scheme, an analysis of the crystal orbital Hamilton population (COHP) [40] has been done based on LMTO-ASA calculations [33, 41]. In [38], distortions of the *B* network of C14-type Laves phases are analyzed analogously, utilizing the crystal orbital overlap population (COOP) method based on extended Hückel calculations. The total density of states of C36 $NbCo_2$ with idealized parameters and the unit cell volume of the title phase has been calculated using FPLO and LMTO-ASA methods.

The DOS (Fig. 13) obtained by the LMTO-ASA calculation matches the FPLO results quite well, especially in the range -1.5 to 2 eV for $E - E_F$. However, the Fermi energy is located on top of a peak in the FPLO-DOS, whereas in the DOS from the LMTO-ASA calculation the peak is shifted slightly below E_F. In the region below -1.5 eV, the LMTO-ASA curve is shifted to slightly lower energies compared to the DOS from FPLO.

Since the LMTO-ASA and full potential calculations are sufficiently in agreement, the bonding situation has been analysed on the basis of COHP calculated by LMTO-ASA results. Three different models have been considered to describe the hypothetical C36 $NbCo_2$ structure:

(i) idealized C36 crystal structure (atomic coordinates from Table 2, ideal c/a ratio) and a unit cell volume (311.33 Å) calculated from that of C15 $NbCo_2$
(ii) idealized C36 crystal structure, unit cell volume (300.96 Å) of the title compound
(iii) atomic coordinates and unit cell parameters of the title compound.

The same atomic sphere radii for Nb and Co have been used in the calculations (ii) and (iii). Selected values of the integrated COHP ($-$ICOHP(E_F)) are given in Table 9.

Assuming the $-$ICOHP(E_F) as a measure of the bond strength, the non-uniform bond strength distribution may be interpreted in all models – based on the results of the total energy calculations and the experimental work – as a tendency towards distortion. Model (i) is in agreement with the bond length order for B_{ij} (Co−Co) obtained from total energy calculations and from experimental work: $B_{11}{}^u < B_{13} < B_{11}{}^c$ and $B_{22} \approx B_{13} \approx B_{23}$. In contrast to the total energy calculations and the experimental work the model (i) indicates $A_{11} > A_{12} \approx A_{22}$. The interatomic distances in model (ii) are slightly shorter due to the smaller unit cell volume induced by the substitution of large Nb atoms by smaller Co atoms. Since values of A_{ij} compared to that of model (i) do not change much, the volume decrease has no serious impact on the bond strengths in the *A* network. It may be concluded, that the contraction of the interatomic distances in the *A* network due to the decrease in unit cell volume is insufficient to enhance both bond strength and distortion. However, there is an increase of the bond strength of the *B* network.

The effect in the *B* network in (iii) is much more pronounced due to the distortion of the structure in this model. In addition, the $-$ICOHP(E_F) indicate now the same bond length order for the A_{ij} as observed by experimental work: $A_{22} < A_{12} < A_{11}$. No data on $-$ICOHP for Nb−Co bonds have been listed in Table 9 since their change is marginal.

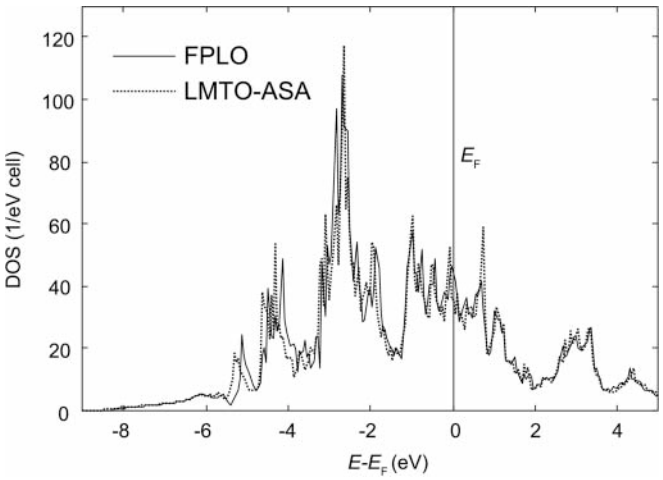

Fig. 13. The total density of states (DOS) calculated for C36 $NbCo_2$ with idealized parameters and the unit cell volume of the title compound by FPLO and LMTO-ASA methods.

Table 8. Interatomic distances $d < 3.20$ Å for C36 $NbCo_2$ obtained on the basis of the hard sphere model (ideal), from total energy calculations (optimized) and for C36 $Nb_{1-x}Co_{2+x}$, $x = 0.265$ (observed). Δ is the relative deviation $100\%[(d/d_{ideal}) - 1]$. Negative and positive values correspond to a contraction and an elongation, respectively.

Type	ideal	optimized		observed	
	d/Å	d/Å	$\Delta_{opt.}$/%	d/Å	$\Delta_{obs.}$/%
$B_{11}{}^u$	2.369	2.357	−0.51	2.324	−1.90
$B_{11}{}^c$	2.369	2.381	0.51	2.417	2.03
B_{22}	2.369	2.369	0.00	2.371	0.08
B_{13}	2.369	2.368	−0.04	2.374	0.21
B_{23}	2.369	2.374	0.21	2.378	0.38
A_{11}	2.902	2.905	0.10	2.935	1.14
A_{12}	2.902	2.905	0.10	2.902	0.00
A_{22}	2.902	2.877	−0.86	2.865	−1.27

Table 9. –ICOHP(E_F) in eV per cell and bond for nearest-neighbor contacts in C36 $NbCo_2$ calculated on the basis of three different models. For a detailed explanation refer to the main text body.

Type	observed	–ICOHP(E_F)		
	d/Å	Model (i)	Model (ii)	Model (iii)
$B_{11}{}^u$	2.324	1.67	1.77	1.91
$B_{11}{}^c$	2.417	1.51	1.61	1.50
B_{22}	2.371	1.57	1.68	1.69
B_{13}	2.374	1.59	1.69	1.68
B_{23}	2.378	1.60	1.70	1.68
A_{11}	2.935	1.22	1.22	1.20
A_{12}	2.902	1.26	1.27	1.26
A_{22}	2.865	1.25	1.26	1.30

Substitutional disorder

Different approaches for the understanding of site preferences have been discussed in the literature. A simple approach is to correlate the volume of a crystallographic site with the observed site occupation. Smaller atoms substitute in general the smaller and lower coordinated site. Voronoi polyhedra (Dirichlet domains) are in general a good measure of the volume of a crystallographic site in intermetallic compounds. However, in $NbCo_2$ with ideal structural parameters the Voronoi polyhedra for both crystallographic Nb sites are equal in volume. Moreover as shown above, both coordination polyhedra for Nb1 and Nb2 are equal.

To gain insight into the origin of the non-uniform distribution of excess Co atoms on Nb sites quantum mechanical calculations have been performed by an all-electron, full-potential method. However, random substitution of Nb atoms by Co atoms prevents a straightforward calculation due to the loss of translational symmetry. Periodicity as required by the Bloch ansatz may be regained by using ordered models as a first approximation to the disordered crystal structure. At least a superstructure with a unit cell of six times the volume of the title compound ($\sqrt{3}a \times \sqrt{3}a \times 2c$) and 144 atoms is required to approximate to some extent the disordered structure. All-electron, full-potential calculations are computationally very demanding in general, and they are not well suited for unit cells containing more than 100 atoms. Therefore, this study has been restricted to a simpler case. Since C36 $Nb_{1-x}Co_{2+x}$ forms close to the composition $NbCo_3$, two Co atoms occupy on average two of the eight Nb positions per unit cell ($Nb_6Co_2Co_{16}$). There are two subgroups of $P6_3/mmc$ which allow for such an ordered arrangement. The 4*f* (M1) and 4*e* (M2) sites of the space group $P6_3/mmc$ split into sites of multiplicity 2 in $P6_3mc$ ($f \rightarrow b^2$, $e \rightarrow a^2$ and $P\bar{6}m2$ ($f \rightarrow ih$, $e \rightarrow g^2$). Models have been calculated using parameters of the idealized and of the refined crystal structure. In the former case Co atoms substitute the Nb atoms at M1 or M2 positions. In the latter case, the Co atoms have been placed at the M1a or the M2a sites. A full treatment of the M1b/M2b sites needs at least the above mentioned supercell. However, the distortion pattern of M1a and M2a is – neglecting the threefold split position – similar to that of the M1b and M2b (see the pattern of arrows in Fig. 10).

Table 10. Total energies of C36 $Nb_6Co_2Co_{16}$ for various ordered models. The energies are listed in units of meV per atom. The total energy of model IIIA is taken as the origin of the energy scale.

Co site	No.	$P6_3mc$	No.	$P\bar{6}m2$
Co@M1	I	11.50	II	38.28
Co@M2	III	4.35	IV	8.76
Co@M1a	IA	15.26	IIA	40.37
Co@M2a	IIIA	0	IVA	5.23

The results of the total energy calculation for idealized (I to IV) and for refined parameters (IA to IVA) are listed in Table 10. The lowest total energy (IIIA) has been taken as the arbitrary origin of the energy scale. Schematic drawings of the respective ordered models as a projection of the Nb network onto the (110) plane are shown in Fig. 14.

The total energy calculations for Co atoms at the M1 or the M2 site reveal the following order of E in meV/atom and E^{III} as arbitrary origin:

$$E^{III}(0) < E^{IV}(4.41) < E^{I}(7.16) < E^{II}(33.93).$$

The total energies of the structures III, IV and I are well below the energy of model II. Obviously, the exchange of Nb–Nb with Co–Co contacts (see Fig. 14) is energetically unfavorable. The distance 2.902 Å for Co–Co pairs occupying Nb sites is 22.5% longer than the nearest neighbor distance of Co atoms in the *B* network. In case of Nb–Co pairs the increase is only 4.5% compared to Nb–Co contacts in $NbCo_2$. Therefore, a high concentration of Co–Co contacts should destabilize the crystal structure due to loss of binding energy. A more detailed analysis is presented in Table 11. Here, the distributions of interatomic distances per unit cell with $d <$ 6.70 Å for the *A* network of models I to IV are listed. It is shown that only model II exhibits Co–Co contacts in the *A* network, whereas the distance distributions for models III, IV and I are equal for nearest and second-nearest neighbors. This explains the small differences in energy between III, IV and I. However, without information on

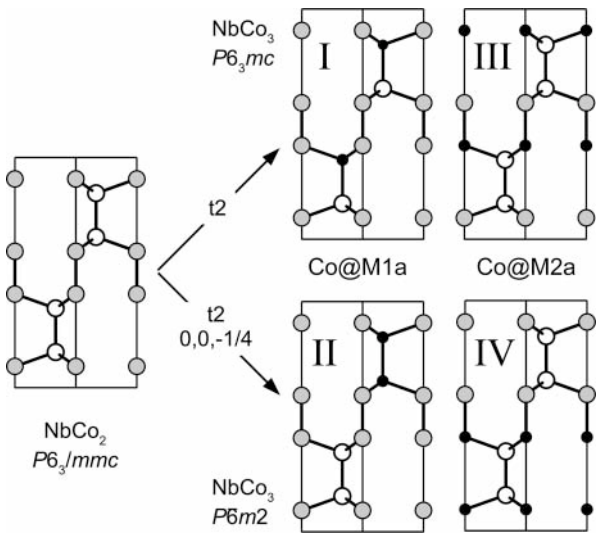

Fig. 14. Projections of the *A* network of C36 $Nb_6Co_2Co_{16}$ with different ordered arrangements of two Co atoms at Nb positions per unit cell. Co atoms are drawn as small, black circles.

Table 11. The distribution of interatomic distances A–A per unit cell with $d < 6.70$ Å for model I to IV ($Nb_6Co_2Co_{16}$). The corresponding distribution for $NbCo_2$ with 108 Nb–Nb pairs per unit cell is: 16×2.902 Å + 48×4.739 Å + 2×4.836 Å + 42×5.557 Å.

	Model I $P6_3mc$, Co@M1			Model II $P\bar{6}m2$, Co@M1			Model III $P6_3mc$, Co@M2			Model IV $P\bar{6}m2$, Co@M2		
d (Å)	Nb–Nb	Nb–Co	Co–Co	Nb–Nb	Nb–Co	Co–Co	Nb–Nb	Nb–Co	Co–Co	Nb–Nb	Nb–Co	Co–Co
2.902	8	8	0	9	6	1	8	8	0	8	8	0
4.739	30	12	6	30	12	6	30	12	6	30	12	6
4.836	2	0	0	2	0	0	0	2	0	1	0	1
5.557	18	24	0	24	12	6	24	18	0	24	18	0

pair potentials the order of energy for the latter models cannot be rationalized in terms of pair interactions. The total energy calculations for Co atoms at the M1a or the M2a site reveal the same order of energies with E in meV/atom and E^{IIIA} as arbitrary origin:

$$E^{IIIA}(0) < E^{IVA}(5.23) < E^{IA}(15.26) < E^{IIA}(40.37).$$

The energy of E^{IIIA} is 4.35 meV below that of E^{III} indicating that displacements of Co atoms at the Nb sites are favorable in energy. There is evidence to suggest a preferred substitution of Nb by Co at M2 sites since for all treated models those ordered structures with Co@M2 are lower in energy than those with Co@M1. A crucial point is that nearest-neighbor interactions cannot explain the effect of the preferential occupation of the M2 site. M1 and M2 are equal with respect to nearest and next-nearest neighbor interactions in case of C36 $NbCo_2$ with ideal structural parameters. However, third- and fourth-nearest interactions are different due to the staggered and eclipsed conformation of M1–M1 and M2–M2 pairs as shown in Fig. 15. A distance of 4.836 Å only occurs between two M2 sites.

The element Co should be the more electronegative element in intermetallic Nb–Co compounds according to the Allred-Rochow atom electronegativity: $\chi(Nb) = 1.23$ and $\chi(Co) = 1.70$. In order to quantify the amount of charge transfer in C36 $NbCo_2$ with idealized structural parameters the atoms-in-molecules concept of Bader [42] has been applied on the basis of the charge density computed by the FPLO method. For the topological analysis of the charge density the program Basin [43] has been used. The atomic basins of Co and Nb atoms contain 27.5 and 40.0 electrons, respectively. The corresponding ionic formula is $Nb^{1+}Co_2^{0.5-}$.

Phase stability of C36 $Nb_{1-x}Co_{2+x}$

According to first principles total-energy calculations, the three polytype structures at stoichiometric composition $NbCo_2$ have almost the same total energy. The calculated ground state energy of C36 $NbCo_2$ is lower than that of C15 $NbCo_2$ by only 0.5 meV per atom. The present phase diagram corroborates older investigations that C15 $NbCo_2$ is stable at the stoichiometric composition up to the melting point. This result is still puzzling and emphasizes the need for further theoretical and experimental investigation concerning the C15 and C14 phases with full optimization. For the calculation of phase equilibria it is necessary to minimize the total Gibbs energy, G, of all the phases that take part in this equilibrium. For a detailed discussion of the phase stabilities including the minimization of the

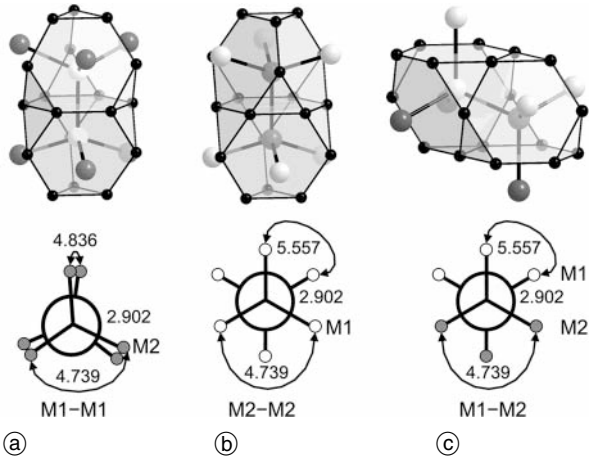

Fig. 15. Staggered and eclipsed conformations of ethane-like (**a**) $M2_3M1$–$M1M2_3$, (**b**) $M1_3M2$–$M2M1_3$, and (**c**) $(M1M2_2)M1$–$M2(M1_2M2)$ units in the crystal structure of C36 $NbCo_2$ with ideal structural parameters. Examples of first-, second-, third-, and fourth-nearest M–M pair distances in Å are indicated.

Gibbs energy reliable experimental data on the homogeneity ranges of C15 and C14 as well as thermodynamic data obtained from calorimetric and thermal analysis techniques are a prerequisite. The discussion here is restricted to a rough estimate of the phase stability of C36 in relation to the binary stoichiometric phase C36 $NbCo_2$. The following chemical reaction describes the formation of Co-rich C36 $Nb_{1-x}Co_{2+x}$ ($\approx NbCo_3$) from C36 $NbCo_2$:

$$(Nb_8Co_{16})_{C36} + 2Co_{hcp} \rightarrow (Nb_6Co_{18})_{C36} + 2\,Nb_{bcc}.$$

The enthalpy of reaction ΔH at 0 K equals the algebraic sum of the ground state energies of products minus the sum of reactants. The ground state energy at the composition $NbCo_3$ has been calculated for the orderly arrangement of model IIIA. For the elements the same set of basis functions and the same exchange-correlation functional have been used in the calculations.

ΔH has been estimated to be 3.2 eV per unit cell (308.8 kJ/mol Nb_6Co_{18}). Since the Gibbs energy ΔG at 0 K is equal to the enthalpy of reaction ΔH the chemical reaction above is not spontaneous. However, at non-zero temperatures entropy may counteract the positive enthalpy. A rough estimate for the entropy change is derived by the following equation describing the Gibbs energy of ideal mixing with the gas constant R, the total number of sites of the sublattice where mixing takes place N^s, and the site fractions y_i^s:

$$G_{mix}^{ideal} = -TS_{mix}^{ideal} = RT \sum_s N^s \sum_i y_i^s \ln y_i^s$$

For ideal mixing of 2 Co atoms onto the 8 Nb sites per unit cell at 1200 K $G_{\mathrm{mix}}^{\mathrm{ideal}} = -44.9$ kJ/mol.

Therefore, the configurational part of the entropy alone is not sufficient to stabilize C36 $NbCo_3$ (model IIIA) with respect to C36 $NbCo_2$. Effects associated with the vibrational part of the entropy and stacking faults (which are readily seen in HREM images [37]) may be important in the stabilization of the title compound with respect to C36 $NbCo_2$. However, the rough calculation above indicates that the C36 $Nb_{1-x}Co_{2+x}$ phase is stable only at high temperatures.

Physical properties

The sample of composition $Nb_{25.2}Co_{74.8}$ shows no field dependence of the magnetic susceptibility $\chi = M(T)/H$ at all for high temperatures and is thus free from ferromagnetic impurities. There are also some paramagnetic moments visible in a Curie-type contribution at low temperatures. $\chi(T)$ of $Nb_{25.2}Co_{74.8}$ is well described by $C/T + \chi_0$ with $C = 0.0032$ emu g^{-1} K and $\chi_0 = +\ 6.7 \cdot 10^{-6}$ emu g^{-1} for $T > 150$ K. The Pauli-paramagnetic contribution after subtraction of the small diamagnetic core contributions ($\chi_{\mathrm{P}} = \chi_0 - \chi_{\mathrm{core}}$) can be estimated to be $+1.31 \cdot 10^{-3}$ emu mol^{-1} ($M = 202.5$ g mol^{-1}).

The magnetic susceptibility $\chi(T)$ of the $Nb_{25.0}Co_{75.0}$ sample is dependent on field in the whole temperature range investigated due to the presence of a minor Co(Nb) phase impurity in the sample (Fig. 16). Traces of the strongly ferromagnetic Co(Nb) phase were also detected in the sample by metallographic examination of the microstructure. An extrapolation of $\chi(1/H)$ to $1/H \rightarrow 0$ yields the corrected curve in Fig. 16. As expected, the curve almost coincides with that of the pure C36 sample.

The electrical resistivity $\varrho(T)$ of $Nb_{25.0}Co_{75.0}$ (Fig. 17) is very high for a binary Laves phase. While the temperature dependent part $\varrho(300\ \mathrm{K}) - \varrho_0$ is only 17 μΩ cm the residual resistivity $\varrho_0 = 140$ μΩ cm is very large confirming a structural (frozen) disorder in the material. For comparison, the residual resistivity of C15 $NbCo_2$ is only

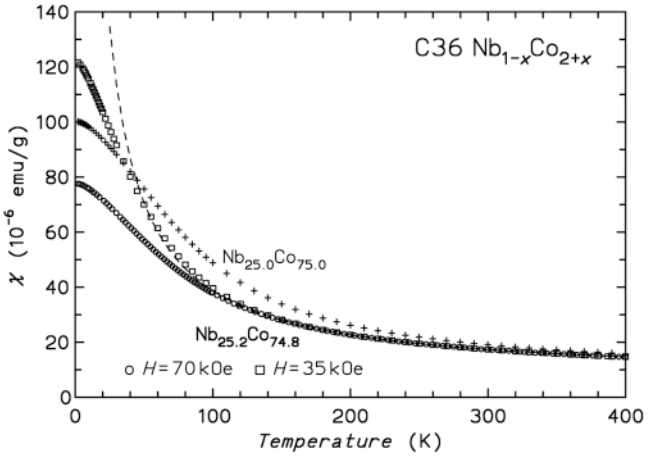

Fig. 16. Magnetic susceptibility $\chi(T)$ of C36 $Nb_{1-x}Co_{2+x}$ samples. For $Nb_{25.2}Co_{74.8}$ the curves for two external magnetic fields and a Curie-type fit (line, see text) and its extrapolation to lower T (dashed line) is shown. For $Nb_{25.0}Co_{75.0}$ the extrapolated data (see text) are displayed.

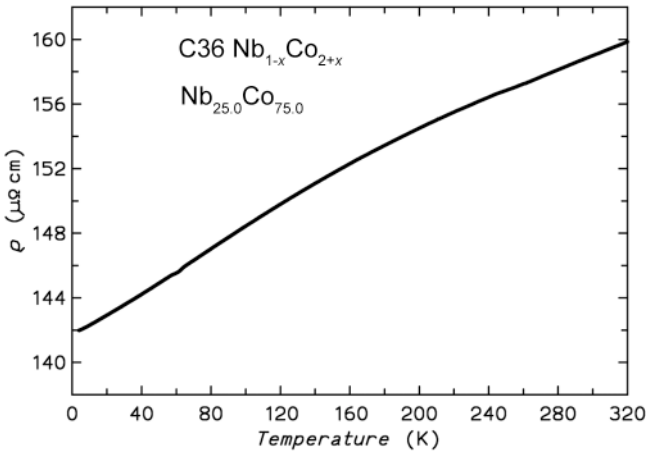

Fig. 17. Electrical resistivity of C36 $Nb_{1-x}Co_{2+x}$ ($Nb_{25.0}Co_{75.0}$ sample).

4 μΩ cm. Interestingly, for temperatures between 5 K and 150 K the temperature dependence $\varrho(T)$ is almost linear, in contrast to simple metals where power laws $\varrho(T) - T^{\alpha}$ with $\alpha > 1$ are usually observed.

Conclusion

A Laves phase with C36 type of structure forms in the Nb–Co system close to the composition $NbCo_3$ as a high temperature phase with a narrow homogeneity range of maximal 0.7(2) at%. The temperature range of the phase field is limited by an eutectoid (C36 = Nb_2Co_7 + C15) and a peritectic (L + C15 = C36) reaction at ≈1050 °C and 1264 °C, respectively. The width of the two-phase field C36 + C15 is smaller than 0.5 at%. From the experimental work of the present study it can be concluded that the C36 Laves phase is an equilibrium phase of the binary system with an off-stoichiometric composition. Structural investigations reveal excess Co atoms substituting the Nb positions in the crystal structure. This substitution is the origin of the deviation from the stoichiometric composition. Vacancies at Nb sites as well as interstitial atoms were not found.

The crystal structure exhibits pronounced deviations from the ideal structural parameters taken from the hard sphere model. The Kagomé layers of hexagonal slabs display an elongation of the edges ($B_{11}{}^{\mathrm{c}}$) of the basal triangles of the Co_5 trigonal bipyramids and a contraction of the edges of the uncapped triangles ($B_{11}{}^{\mathrm{u}}$). The distortion pattern is in agreement with those found for the majority of C14 and C36 Laves phases whose atomic positions have been refined. Based on quantum mechanical calculations it was shown that the distortion crystal structure is a consequence of the bonding situation of the defect-free crystal structure. The full potential calculations reveal a tendency for a distortion of the idealized crystal structure.

The local ordering and atomic displacements were detected by single crystal structure refinements. From total energy calculations it can be concluded that the local displacements in combination with entropy effects are very important to stabilize the crystal structure of the C36 type with respect to stoichiometric C36 and C15 $NbCo_2$.

The Co atoms substitute Nb atoms randomly. No superstructure describing any kind of an ordered arrangement has been observed. Co atoms exhibit a site preference for the M2 positions. Here, approximately twice as much Co substitutes Nb compared to the M1 site. Due to the tiny homogeneity range the same conclusion still holds for Co or Nb saturated C36 phases. The full potential calculations corroborate the assumption that the tendency for the preferential site occupation is an inherent feature of the C36 structure type in the Nb–Co system. Since both crystallographic Nb sites in stoichiometric $NbCo_2$ are equivalent with respect to nearest-neighbor interactions the difference must be due to interactions with atoms beyond the first and second coordination shells. However, distortions and local displacements may have an influence on the magnitude of the effect. The C36 phase $Nb_{1-x}Co_{2+x}$ is a Pauli-paramagnetic metal with a high residual resistivity.

Acknowledgments. We are thankful to the following colleagues: Dr. Y. Prots and Mr. S. Hückmann (X-ray measurements), Dr. G. Auffermann, Ms. U. Schmidt, and Ms. A. Völzke (chemical analyses), Dr. U. Burkhardt and Ms. M. Eckert (metallography), Mr. R. Koban (measurements of magnetization and electrical resistivity), Dr. R. Ramlau and Ms. K. Schulze (SEM, EDXS, and WDXS).

References

[1] Friauf, J. B.: The crystal structure of two intermetallic compounds. J. Am. Chem. Soc. **49** (1927) 3107–3114.
[2] Friauf, J. B.: The crystal structure of magnesium dizincide. Phys. Rev. **29** (1927) 34–40.
[3] Laves, F.; Witte, H.: Die Kristallstruktur des $MgNi_2$ und seine Beziehung zu den Typen des $MgCu_2$ und $MgZn_2$. Metallwirtschaft **14** (1935) 645–649.
[4] Laves, F.; Witte, H.: Der Einfluss der Valenzelektronen auf die Kristallstruktur ternärer Magnesium-Legierungen. Metallwirtschaft **15** (1936) 840–842.
[5] Schulze, G. E. R.: Zur Kristallchemie der intermetallischen AB_2-Verbindungen (Laves-Phasen). Z. Elektrochem. **45** (1939) 849–865.
[6] Frank, F. C.; Kasper, J. S.: Complex alloy structures regarded as sphere packings. I. Definitions and basic principles. Acta Crystallogr. **11**(3) (1958) 184–190.
[7] Frank, F. C.; Kasper, J. S.: Complex alloy structures regarded as sphere packings. II. Analysis and classification of representative structures. Acta Crystallogr. **12**(7) (1959) 483–499.
[8] Jagodzinski, H.: Der Symmetrieeinfluss auf den allgemeinen Lösungsansatz eindimensionaler Fehlordnungsprobleme. Acta Crystallogr. **7** (1954) 17–25.
[9] Samson, S.: Development in the Structural Chemistry of Alloy Phases. (B.C. Giessen, ed.) Plenum Press, New York, 1969.
[10] Thoma, D. J.; Perepezko, J. H.: A geometric analysis of solubility ranges in Laves phases. J. Alloys Compd. **224** (1995) 330–341.
[11] Stein, F.; Palm, M.; Sauthoff, G.: Structure and stability of Laves phases. Part I. Critical assessment of factors controlling Laves phase stability. Intermetallics **12** (2004) 713–720.
[12] Stein, F.; Palm, M.; Sauthoff, G.: Structure and stability of Laves phases Part II. Structure type variations in binary and ternary systems. Intermetallics **13** (2005) 1056–1074.
[13] Köster, W.; Mulfinger, W.: Die Systeme des Kobalts mit Bor, Arsen, Zirkon, Niob und Tantal, Z. Metallkd. **30** (1938) 348–350.
[14] Wallbaum, H. J.: Ergebnisse der röntgenographischen Strukturuntersuchung von Legierungen der Zusammensetzung AB_2 der Eisenmetalle mit Titan, Zirkon, Niob und Tantal. Z. Kristallogr. **103** (1941) 391–402.
[15] Saito, S.; Beck, P. A.: Co-Rich Intermediate Phases in the Nb–Co System. Trans. Metall. Soc. AIME **218** (1960) 670–674.
[16] Raman, A.: X-ray investigation in the Niobium–Cobalt System, Trans. Metall. Soc. AIME **236** (1966) 561–565.
[17] Pargeter, J. K.; Hume-Rothery, W.: The constitution of the Niobium–Cobalt system, J. Less-Common Met. **12** (1967) 366–374.
[18] Bataleva, S. K.; Kuprina, V. V.; Markiv, V. Y.; Burnashova, V. V.; Ronami, G. N.; Kuznetsova, S. M.: Cobalt-Niobium Phase-Diagram, Trans. Moscow State Univ. Ser. Chim. **25**(4) (1970) 37–40.
[19] Massalski, T. B.: Binary Alloy Phase Diagramms. Second Edition (T. B. Massalski, ed.) ASM International, Materials Park, Ohio, 1990, p. 1211.
[20] Hari Kumar, K. C.; Ansara, I.; Wollants, P.; Delaey, L.: Thermodynamic Optimisation of the Co–Nb System. J. Alloys Compd. **267** (1998) 105–112.
[21] Okamoto, H.: Co–Nb (Cobalt–Niobium). J. Phase Equilibria **21** (2000) 495.
[22] Gabe, E. J.; Le Page, Y.; Charland, J. P.; Lee, F. L.; White, P. S.: NRCVAX – An Interactive Program System for Structure Analysis, J. Appl. Crystallogr. **22** (1989) 384–387.
[23] Stoe WINXPOW 1.2, Stoe & Cie GmbH, Darmstadt 2001.
[24] Rigaku MSC, CrystalClear-Software, Version 1.3.6SP0, 2004.
[25] Sheldrick, G. M.: SHELXL97–2, Program for the Solution and Refinement of Crystal Structures. University of Göttingen, 1997.
[26] Akselrud, L. D.; Zavalii, P. Y.; Grin, Y.; Petcharski, V. K.; Baumgartner, B.; Wölfel, E.: Use of the CSD program package for structure determination from powder data. Mater Sci. Forum **335** (1993) 133–136.
[27] Petricek V.; Dusek M.: Jana2000. The crystallographic computing system. Institute of Physics, Praha, Czech Republic, 2000.
[28] Köpernik, K.; Eschrig, H.: Full-potential nonorthogonal local-orbital minimum-basis band-structure scheme. Phys. Rev. B**59**(3) (1999) 1743–1757.
[29] Kohn, W.; Sham, L. J.: Self-consistent equations including exchange and correlation effects. Phys. Rev. **140** (1965) A1133–A1138.
[30] Hohenberg, P.; Kohn, W.: Inhomogeneous electron gas. Phys. Rev. **136** (1964) B864–B871.
[31] Eschrig, H.: Optimized LCAO Method and the Electronic Structure of Extended Systems. Springer, Berlin, 1989.
[32] Perdew, J. P.; Wang, Y.: Accurate and simple analytic representation of the electron-gas correlation energy. Phys. Rev. B**45** (1992) 13244–13249.
[33] Krier, G.; Jepsen, O.; Burkhard, A.; Andersen, O. K.: Tight Binding LMTO-ASA Program. Version 4.7, Stuttgart, Germany 1998.
[34] Williams, D. S.; Rapp, R. A.; Hirth, J. P.: Phase suppression in the transient stages of interdiffusion in thin-films. Thin Solid Films **142** (1986) 47–64.
[35] Gelato, L. M.; Parthé, E.: Structure Tidy – a computer program to standardize crystal structure data. J. Appl. Crystallogr. **20** (1987) 134–139.
[36] Allen, C. W.; Delavignette, P.; Amelinckx, S.: Electron microscopic studies of the Laves phases $TiCr_2$ and $TiCo_2$. Phys. Stat. Sol. (a) **9** (1972) 237–246.
[37] Yokosawa, T.; Söderberg, K.; Boström, M.; Grüner, D.; Kreiner, G.; Terasaki, O.: Microscopic structures of Laves phases and structurally related compounds: A transmission electron microscopy study. Z. Kristallogr. **221** (2006) 357–374.
[38] Johnston, R. L.; Hoffmann, R.: Structure-bonding relationships in the Laves phases. Z. Anorg. Allg. Chem. **616** (1992) 105–120.
[39] Vold, C. L.: The crystal structure of $NbZn_2$. Acta Crystallogr. **14** (1961) 1289–1290.
[40] Dronskowski, R.; Blöchl, P. E.: Crystal Orbital Hamilton Populations (COHP) – energy resolved visualization of chemical bonding in solids based on density-functional calculations. J. Phys. Chem. **97** (1993) 8617–8624.
[41] Boucher, F.; Jepsen, O.; Andersen, O. K.: Supplement to the LMTO-ASA Program Version 4.7. Nancy, France, 1997.
[42] Bader, R. F. W.: Atoms in Molecules – A Quantum Theory, Clarendon Press, Oxford, 1995.
[43] Kohout, M.: Program Basin, Version 2.4. Max-Planck-Institut für Chemische Physik fester Stoffe, Dresden, Germany, 2004.